nature communications

Article

https://doi.org/10.1038/s41467-026-69431-y

Phosphorescent supramolecular systems for medicine anticounterfeiting

Received: 26 June 2025

Accepted: 2 February 2026

Published online: 11 February 2026

Check for updates

Wen-Ting Wu[1,3], Chun-Yun Deng[1,3], Zhi-Yuan Zhang[1] ✉, Yue-Yi Zhang[1], Kun Liu[1] ✉, Yanli Zhao[2] ✉ & Chunju Li[1] ✉

Realizing reliable medicine anticounterfeiting with safe and robust materials remains a challenge. We address this issue by preparing a class of edible phosphorescent supramolecules (VB10@α/β-CDs) based on easily available α/β-cyclodextrins (α/β-CDs) and vitamin B10 (VB10). Concisely grinding them with water or co-crystallization from aqueous solution, the resulting host–guest complexes VB10@α/β-CDs exhibit a long phosphorescence lifetime of up to 1.16 s and a high photoluminescent quantum yield of up to 86.5%, The encapsulation of α/β-CDs reverses the energy ordering of VB10's excited singlet states, promotes the formation of the minimum energy crossing point (MECP) between singlet state and triplet state, and therefore boosts phosphorescence. VB10@α/β-CDs are attractive as phosphorescent inks for in-medicine anticounterfeiting because of the advantages of an edible nature, good moisture robustness, room-temperature phosphorescence and circularly polarized luminescence. Therefore, the present phosphorescent supramolecules as well as the elucidated MECP-involved mechanism would promote in-depth understanding of phosphorescence enhancement strategy.

Counterfeiting medicines are a tremendous threat to patient safety and public health[1,2]. More than 280,000 children in sub-Saharan Africa die every year because of counterfeiting and substandard medical products[2]. The involved medicine is worth up to US$100 billion all over the world[3]. Chemical analysis and chromatography/spectroscopy technologies for pharmaceutical ingredient detection, and anticounterfeit methods at the packaging level are commonly used to combat counterfeiting medicines[4–8]. These methods work well with preconditions that expensive experiments/skilled personnel were equipped or that the drugs are not repackaged. In-medicine anticounterfeiting (or in-dose authentication) is a more advanced and effective method because every individual pill or capsule is verified independently of the packaging[6,7,9–11]. Within this set, encrypting and printing information on the surface of pills and capsules by luminescent materials is particularly attractive due to low cost and intuitive detection[11–14]. However, there are still no perfect luminescent materials for ink marking because of the strict requirements of in-medicine anticounterfeiting, such as non-toxic preferably edible, high signal-to-noise ratio of luminescence, and good robustness under ambient conditions.

Cyclodextrins (CDs)[15,16] are widely used pharmaceutical excipients and are recognized as edible macrocyclic molecules[17,18]. The hydrophilic surface and hydrophobic cavities make CDs excellent water-soluble macrocyclic hosts for encapsulating various organic guests[16,19–21]. Pioneering works have demonstrated that the encapsulation can usually alter the physical and chemical properties of guests[22–28]. Vitamin B10 (VB10) is an essential component of the folate, which is necessary for cellular growth and differentiation[29,30]. It is sold as an essential nutrient when normal synthesis by intestinal bacteria is insufficient. Although VB10 exhibited a weak blue fluorescence, the theoretical calculations showed that it has multiple singlet states and triplet state (Supplementary Figs. 1–6). We postulated that it would be

[1]Academy of Interdisciplinary Studies on Intelligent Molecules, Tianjin Key Laboratory of Structure and Performance for Functional Molecules, College of Chemistry, Tianjin Normal University, Tianjin, P. R. China. [2]School of Chemistry, Chemical Engineering and Biotechnology, Nanyang Technological University, 21 Nanyang Link, Singapore, Singapore. [3]These authors contributed equally: Wen-Ting Wu, Chun-Yun Deng. ✉e-mail: zzy@tjnu.edu.cn; hxxyliuk@mail.tjnu.edu.cn; zhaoyanli@ntu.edu.sg; cjli@shu.edu.cn

https://doi.org/10.1038/s41467-026-69431-y

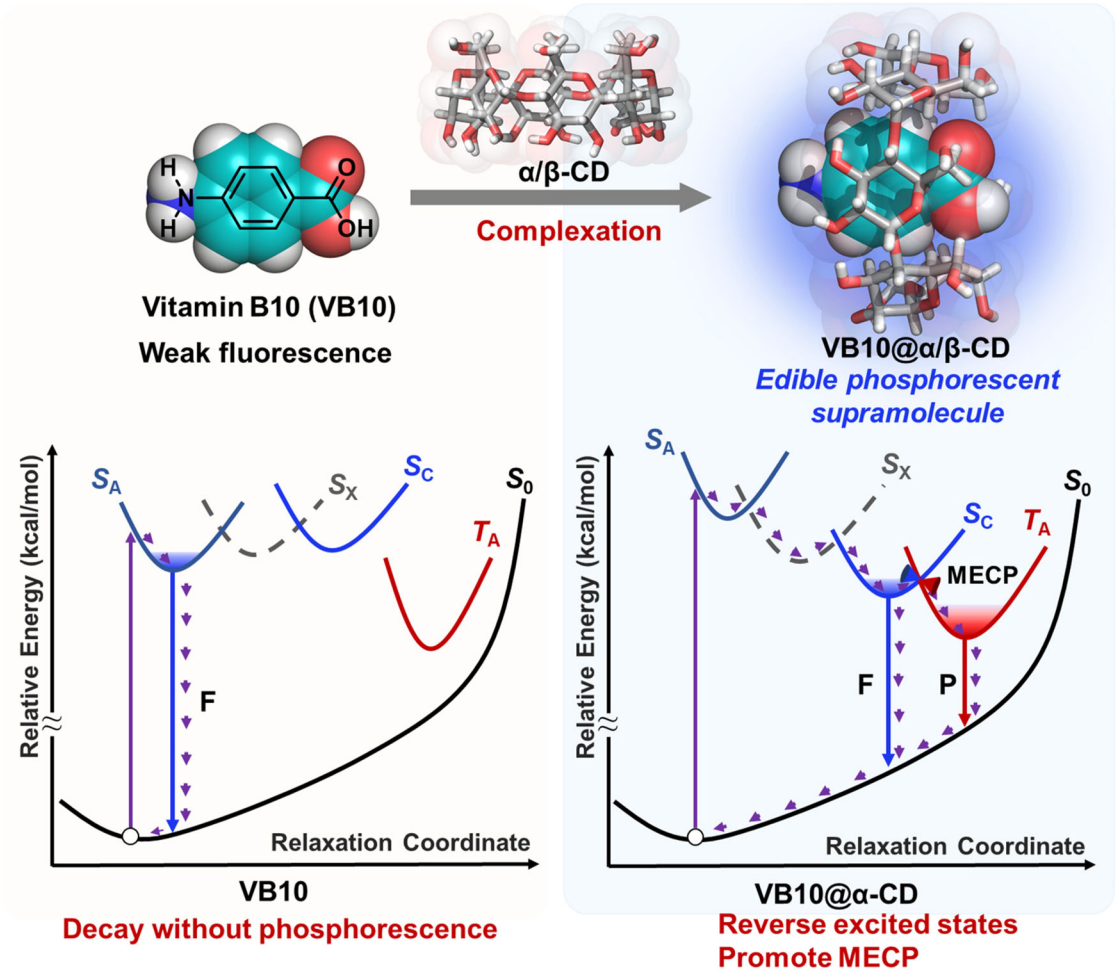

Fig. 1 | Structures and photoluminescent mechanisms. Schematic illustration for the preparation of edible phosphorescent supramolecules from α/β-CD and VB10 as well as the photoluminescent mechanisms.

possible to regulate its excited state to induce room-temperature phosphorescence (RTP) and produce a good phosphorescent ink-marking material by encapsulating with CDs. RTP has a reputation of long persistent luminescence after ceasing irradiation, which endow RTP materials intrinsic advantages for anticounterfeiting[12,31,32]. In particular, the well-developed constructing strategies for RTP materials provided enriched toolbox for designing and preparing RTP anticounterfeiting materials, such as crystallization engineering[33–37], doping into matrix[38–41], polymerization[33,42–44], self-assembly[45–47], host-guest interactions[48–51], and etc[52,53].

In addition, quantum chemistry calculations have been proven to be important tools for expounding on the underlying mechanisms of luminescent materials[54,55]. The calculation of absorption spectra is well-established[56], and the HOMO/LUMO energy levels of the ground state are commonly used to infer the properties of excited states[57,58]. However, revealing the luminescence mechanism through calculations, particularly for large organic molecular systems or even organic supramolecular systems, remains a significant challenge. Understanding the complete photophysical processes and the dominant decay pathways is essential for identifying the key factors that influence luminescence and for designing improved luminescent materials. The interactions between electron spin and orbital angular momentum, as well as between electrons and atomic nucleus, lead to complex low-lying excited-state crossings and multiple decay pathways for the excited molecules[59,60]. Theoretically, while multi-reference methods offer higher accuracy, they make the quantitative calculation of photophysical processes for large systems expensive and complex, thus difficult to accomplish. Therefore, it is of great significance to develop a computational strategy that is suitable for large organic molecule/supramolecule system in the solid state.

Herein, two edible phosphorescent supramolecules, namely VB10@α-CD and VB10@β-CD, are facilely prepared by grinding VB10 and α/β-CD with water or co-crystallizing them from aqueous solution (Fig. 1). The resulting supramolecules show a photoluminescence quantum yield of up to 86.5%, a lifetime of up to 1.16 s, a visible afterglow lasting for 6 s, and good robustness in ambient conditions. The edible VB10@α-CD as phosphorescent ink-marking material is applied in the in-medicine anticounterfeiting. Moreover, we specifically develop a computational approach that combines single-reference time-dependent density functional theory (TDDFT) with the ONIOM model, with a focus on the minimum energy crossing point (MECP), to investigate the luminescence mechanism of VB10@α-CD. The computational results not only agree with the experimental data, but also offer clear insights into the distinct luminescent behavior of VB10@α-CD in both solution and the solid state. The crucial roles of non-radiative processes for phosphorescence are clearly revealed. The hydrogen bonds provided by CD regulate singlet states (S_n) of VB10, promote the formation of MECP between singlet state S_c and triplet state T_1, and therefore boost phosphorescence. Thus, phosphorescent supramolecules VB10@α/β-CDs are suitable systems that combine edibility, low cost, high performance, robustness, and a fully elucidated solid-state phosphorescence mechanism. The phosphorescent supramolecular ensemble represents a paradigm for developing phosphorescent materials, which may find promising utility in high-

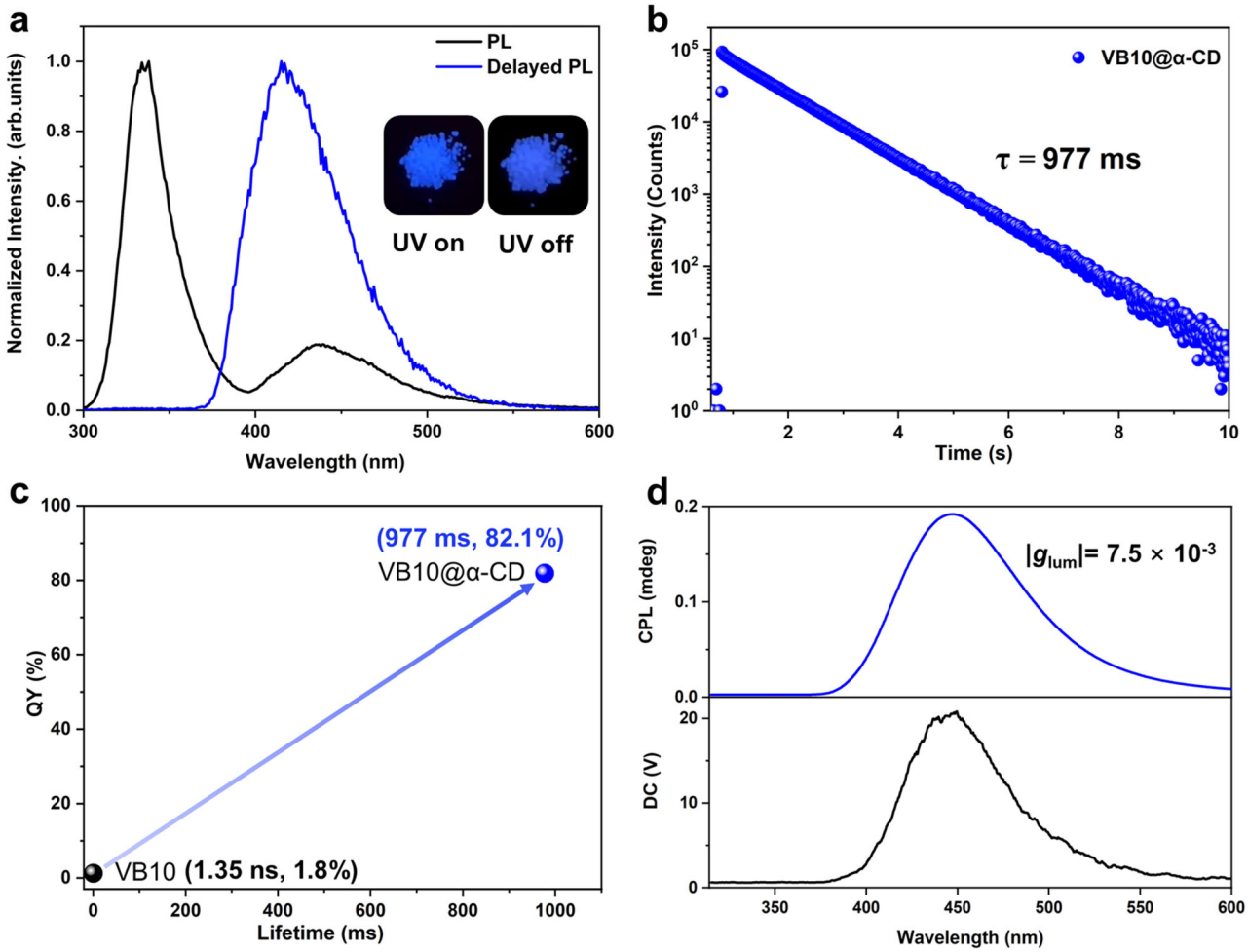

Fig. 2 | Photophysical properties of VB10@α-CD in the crystal state. a PL spectra (black) and delayed PL spectra (blue) of VB10@α-CD (Inset: luminescence photographs of VB10@α-CD crystals under 254 nm and after ceasing irradiation). **b** Time-resolved PL decay curves of VB10@α-CD at 298 K. **c** Measured lifetimes and quantum yields of VB10, α-CD, and VB10@α-CD. **d** CPL spectrum of VB10@α-CD at 298 K.

security anticounterfeiting scenario within the pharmaceutical industry.

Results

The VB10 itself exhibited weak blue fluorescence (λ_{max} = 404 nm) with a lifetime (τ) of 1.35 ns and a photoluminescence quantum yield (PLQY) of 1.8% (Supplementary Figs. 2 and 3). After grinding it with α-CD, which is known as a nonluminous macrocycle, the obtained VB10/α-CD displayed intense blue emission and a bright blue afterglow lasting up to 4 s with a lifetime of 210 ms and PLQY of 16.5% under ambient condition (Supplementary Figs. 7 – 10). This result indicated that α-CD could "turn on" the phosphorescence of VB10. After dissolving the VB10/α-CD into water and slowly evaporating for 6 days, the obtained single crystal of VB10/α-CD showed a longer blue afterglow (Fig. 2a and Supplementary Fig. 11). The photoluminescence (PL) spectra, delayed PL spectra, and time-resolved PL decay curves indicated that the afterglow is phosphorescence (λ_{max} = 434 nm) with a lifetime of 977 ms, along with fluorescence peak at 340 nm (τ = 1.38 ns) (Figs. 2a, b and Supplementary Fig. 12). Notably, the PLQY of VB10@α-CD is up to 82.1%, indicated the great promotion of α-CD for the phosphorescence of VB10 (Fig. 2c and Supplementary Fig. 13). The longer lifetime and higher PLQY of crystals than that of grinded samples are probably because of better encapsulation of α-CD for VB10. The high-performance luminescence in ambient conditions proved its good robustness and provided an essential requirement for applications.

Since α-CD is a macrocycle possessing a chiral cavity, it is speculated that the chiral transfer between α-CD and VB10 may induce circular dichroism and circularly polarized luminescence (CPL) signals[26–28]. The circular dichroism spectrum of solid VB10@α-CD features a stronger positive Cotton effect at 335 nm compared with that in aqueous solution (Supplementary Fig. 14). As shown in Supplementary Fig. 15, the VB10@α-CD exhibited positive distinct dual CPL including fluorescence (λ_{max} = 340 nm) and phosphorescence (λ_{max} = 440 nm), with $|g_{lum}|$ values of 1.5×10^{-2} and 7.5×10^{-3}, respectively. Considering the high PLQY, long lifetime, and relatively high $|g_{lum}|$ values, the VB10@α-CD is among the high-performance organic RTP systems with CPL property (Supplementary Table 1). The phosphorescent CPL was further proven by the intense emission of CPL measurement in phosphorescence mode (Fig. 2d and Supplementary Fig. 16). These results verified that the chiral transfer from α-CD to VB10 could produce CPL. The relationship between the host–guest molar ratios and the phosphorescent properties of VB10/α-CD was further evaluated. When the molar ratios of VB10: α-CD increased from 1:1 to 1:1000, the afterglow remained and the PL spectra showed a slightly blueshift from 340 nm to 331 nm, which probably due to more completed encapsulation for VB10 (Supplementary Fig. 17a, b). The identical PL spectra of VB10@α-CD at 1:100 and 1:1000 revealed that VB10 was encapsulated by α-CD in these molar ratios. More α-CD probably translated more VB10 into the supramolecule VB10@α-CD, and therefore exhibited stronger emission. The phosphorescence

https://doi.org/10.1038/s41467-026-69431-y

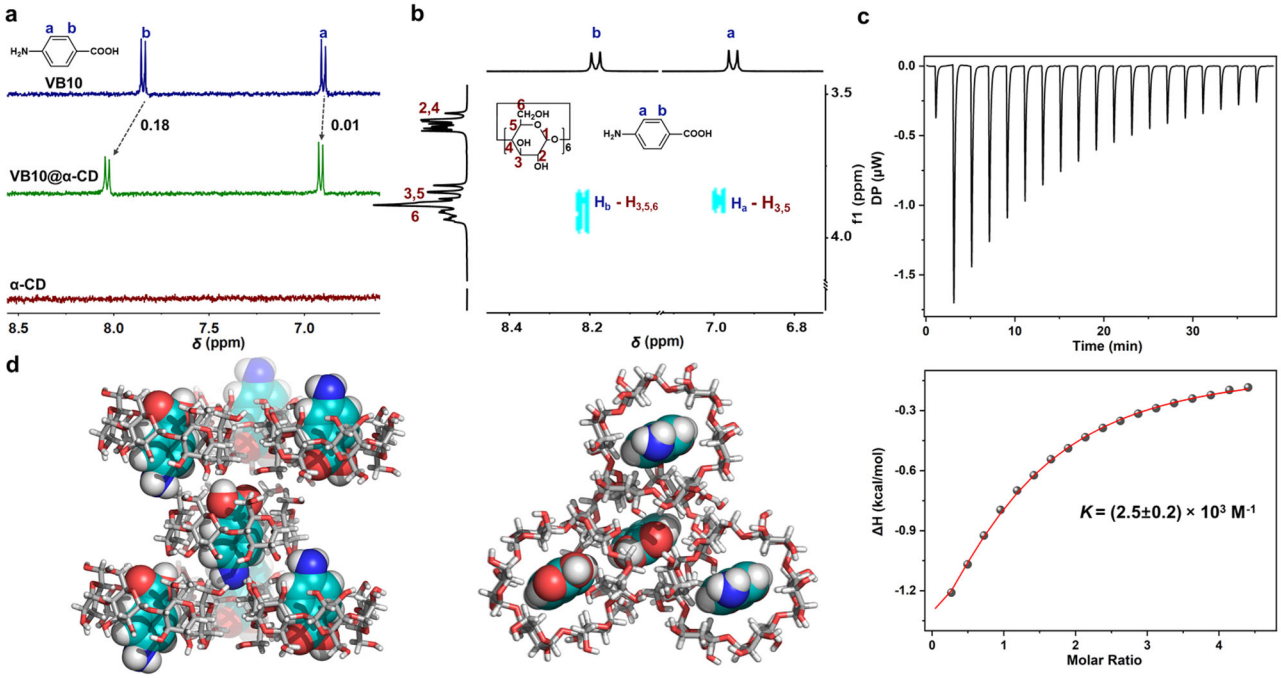

Fig. 3 | Host–guest properties of VB10@α-CD. a ^{1}H NMR (400 MHz, D_2O, 298 K) spectra of VB10, VB10@α-CD and α-CD ([α-CD] = 2[VB10] = 2×10^{-3} mol/L). **b** A section of ^{1}H-^{1}H NOESY NMR spectrum (400 MHz, D_2O, 298 K) of VB10@α-CD ([α-CD] =2[VB10] = 2×10^{-2} mol/L). **c** ITC titration data of α-CD titrated into VB10 ([VB10] = 3.5×10^{-4} mol/L, [α-CD] = 8.0×10^{-3} mol/L). **d** Single-crystal structures of VB10@α-CD (Front view and top view). α-CD and VB10 are illustrated as stick and space-filling representations, respectively.

lifetimes were at a range of 214 − 302 ms and PLQY increased from 16.5% for 1:1 to 33.2% for 1:1000, indicating that better encapsulation might occur by increasing the molar ratio of α-CD (Supplementary Figs. 17c,17d and 18). It was hypothesized that this phosphorescence enhancement could be due to the encapsulation of α-CD for VB10.

The encapsulation of α-CD for VB10 was verified by ^{1}H NMR and ^{1}H − ^{1}H NOESY NMR spectroscopy, isothermal titration calorimetry (ITC), and X-ray single crystal diffraction analysis. The protons H_a and H_b in VB10 showed downfield shifts of 0.01 and 0.18 ppm, respectively, after the addition of 2 equiv α-CD (Fig. 3a and Supplementary Fig. 19). This is a typical complexation-induced shift because of the hydrogen-bonding between CD and guests, proving the encapsulation and verifying that VB10/α-CD is the supramolecular complex VB10@α-CD. In the ^{1}H − ^{1}H NOESY NMR spectra of VB10@α-CD, cross-peaks between $H_a - H_{3,5}$ and $H_b - H_{3,5,6}$ provided evidence for the close proximity between the phenyl group of the VB10 and the cavity of the α-CD, suggesting a deep encapsulation mode (Fig. 3b and Supplementary Fig. 20). ITC gave a binding constant (K_a) of $(2.5 \pm 0.2) \times 10^3$ M^{-1}, accompanying with favorable enthalpy change and positive entropy contribution (Fig. 3c). Diffraction grade single crystals of VB10@α-CD were obtained as colorless block through the slow evaporation of an aqueous solution containing the α-CD and VB10 (1:1) at room temperature for 6 days. The resulting single-crystal structures were shown in Fig. 3d with associated data given in Supplementary Table 2. VB10 is deeply located into the cavity of α-CD, with COOH and NH_2 groups pointing into the primary face and secondary face, respectively. The dihedral angle between the plane of the phenyl in VB10 and the cross-section formed by six glycosidic oxygen atoms in α-CD is 86.4°, revealing a vertical encapsulating manner for VB10 (Supplementary Fig. 21)[61]. The host–guest complexes stacked in register to form supramolecular structures. Furthermore, the COOH and NH_2 groups formed multiple hydrogen bonds with its host α-CD and adjacent α-CD (1.68, 1.90, 2.00, 2.01, 2.07, 2.12, 2.17, 2.45, 2.54, and 2.91 Å) (Supplementary Fig. 22). Thus, the reason of robust phosphorescence in ambient conditions is clearer. Normally, the triplet states T_n (n ≥ 1) of phosphor suffer serious quenching even by a very low concentration of oxygen, water, impurities, or aggregation-caused quenching (ACQ) because of triplet energy migration. In the case of supramolecule VB10@α-CD, host α-CD acted as a good shell to shelter the chromophoric core (VB10) by suppressing the above quenching and therefore stabilized the triplet states T_n (n ≥ 1). Furthermore, every VB10 molecule in the VB10@α-CD supramolecule is in an individual microenvironment provided by α-CD, making each host–guest complex an independent phosphor unit. Possible defects (empty α-CD or free VB10) would not cause serious triplet energy migration and therefore had little effect on the whole phosphorescent performance. Collectively, these advantages promoted the robust phosphorescence of VB10@α-CD under ambient conditions.

To further elucidate the origin of phosphorescence in the solid state, we employed quantum mechanical calculations for VB10@α-CD (Supplementary Figs. 23–32). The ONIOM model was utilized, treating α-CD as the surrounding environment, to carry out the simulations using the PM6 semi-empirical method with D3 dispersion correction, while the core VB10 was calculated using the PBE0(GD3BJ)/6-31 G* method. The detailed dynamics of the excited states were analyzed as follows: First, the ground state structure ($S_{0\ min}$) was fully optimized. Subsequently, vertical excitation energies were computed using the TDA method, identifying the excited states corresponding to the main experimental absorption. Finally, the dynamics of the transition from the main excited states to the triplet state associated with phosphorescence was quantitatively described. The dominant electronic transitions of the three important low-lying excited singlet states are shown in Fig. 4a, and Supplementary Figs. 33–36, and Supplementary Data 1. Due to the very small energy differences among them and variable relative location, conventional naming rules such as S_1, S_2 and S_n are unsuitable. Therefore, we designated these states as singlet state A (S_A, $f = 0.5364$), singlet state B (S_B, $f = 0.0025$), and singlet state C (S_C, $f = 0.0003$) based on their oscillator strength values (f). Among these, S_A corresponds to the main absorption band.

https://doi.org/10.1038/s41467-026-69431-y

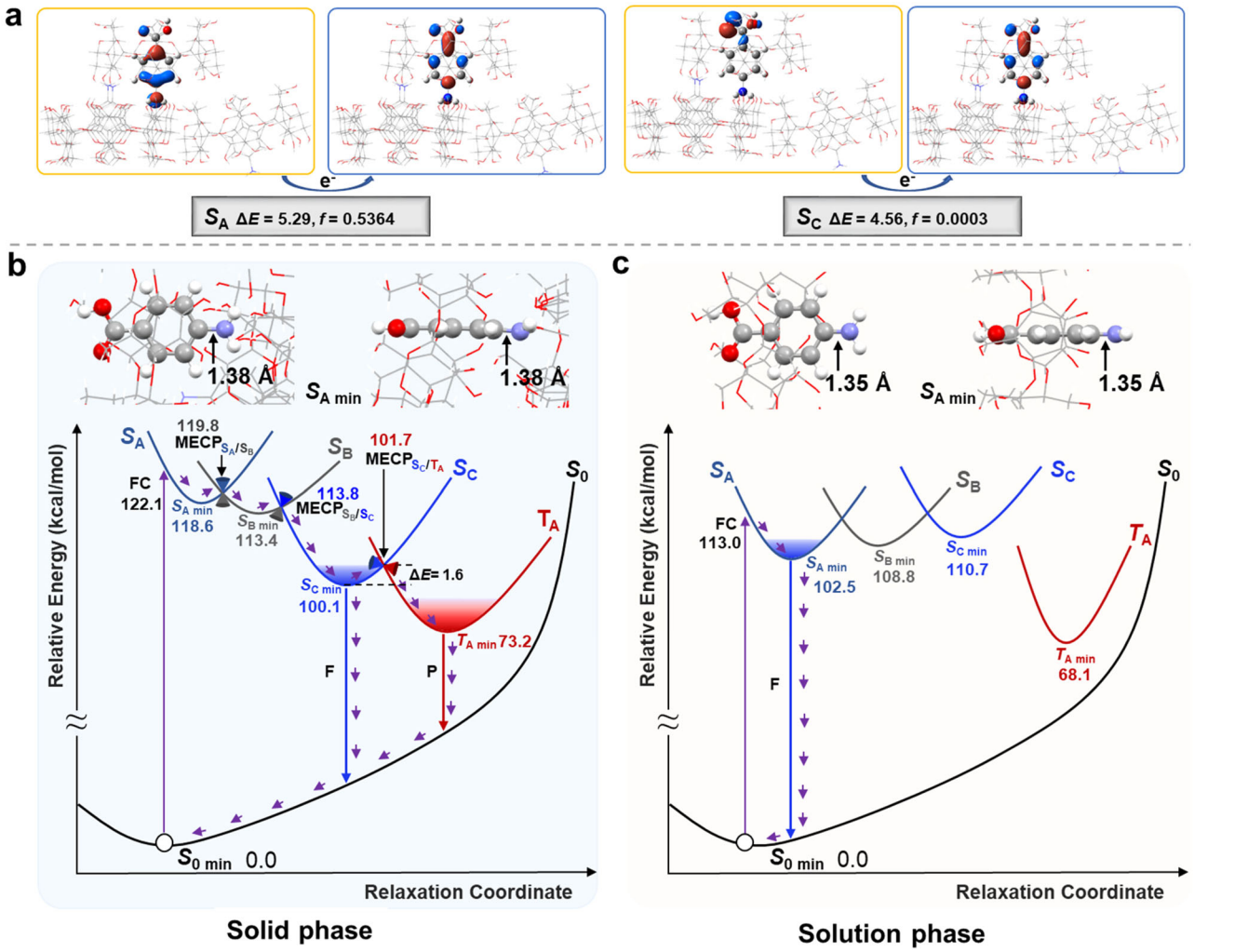

Fig. 4 | Calculation results. a Electronic structures (S_A and S_C) of low-lying excited states involved in relaxation processes calculated at TDA-PBE0/PBE0/6-31 G* level of VB10@α-CD in solid-phase ONIOM model. *f* represents the oscillator strength, and Δ*E* denotes the energy gap in eV. **b**, **c** Radiative and nonradiative relaxation processes of VB10@α-CD in (**b**) solid-phase ONIOM model and (**c**) solution phase (Inset: the minimum energy structures (top view and side view) of VB10@α-CD in the most stable low-lying excited singlet state of S_A ($S_{A\ min}$).

The nonradiative relaxation process of VB10@α-CD in the solid-phase ONIOM model is depicted in Fig. 4b, starting from the Frank-Condon point, passing through minimum energy crossing points ($MECP_{SA/SB}$ and $MECP_{SB/SC}$), and crossing two very small energy barriers (1.2 kcal/mol between $S_{A\ min}$ (118.6 kcal/mol) and $MECP_{SA/SB}$ (119.8 kcal/mol), and 0.4 kcal/mol between $S_{B\ min}$ (113.4 kcal/mol) and $MECP_{SB/SC}$ (113.8 kcal/mol)). Based on the small barrier, we infer that VB10@α-CD is likely to reach the lowest-energy stationary point ($S_{C\ min}$, 100.1 kcal/mol) among all excited singlet states very quickly, and subsequently emit fluorescence at 375 nm, which is similar with the experimental data of 340 nm. Subsequently, VB10 can cross a very small energy barrier of 1.6 kcal/mol via $MECP_{SC/TA}$ (101.7 kcal/mol), reaching the stable minimum point of low-lying excited triplet state T_A ($T_{A\ min}$, 73.2 kcal/mol) (Supplementary Fig. 37). Then, it relaxes from $T_{A\ min}$ to S_0 and emits phosphorescence at 426 nm, which is well matched with the experimental data of 434 nm. Figure 4b indicates that the presence of an $MECP_{SC/TA}$ is a key factor for phosphorescence in the solid state by facilitating the relaxation from the S_C to T_A. In contrast, in aqueous solution, $S_{A\ min}$ is the lowest stationary point among all low-lying excited singlet states, and $MECP_{SA/TA}$ is not obtained through our calculations (Fig. 4c and Supplementary Figs. 38–42). This is consistent with experimental result that no phosphorescence could be detected in the aqueous solution (Supplementary Fig. 43).

This discrepancy can be clarified by two factors: First, $S_{C\ min}$ is the lowest stationary point among all low-lying excited singlet states in the solid state, while $S_{A\ min}$ is the lowest-energy excited singlet state in the aqueous solution. The reversed energy order of $S_{A\ min}$ and $S_{C\ min}$ in the solid-phase ONIOM model and solution phase can be understood by examining the structures of $S_{A\ min}$ in both phases. In the solution phase, the orbital responsible for electron donation in S_A excitation exhibits a pronounced antibonding characteristic in the C-N region (Supplementary Fig. 38), leading to a shortening of the C-N bond (1.35 Å) in $S_{A\ min}$ compared to the ground state ($S_{0\ min}$) (1.36 Å) (Supplementary Figs. 44 and 45). The structure of $S_{A\ min}$ shows that the amino and phenyl groups are in a coplanar arrangement due to conjugation, which is energetically favorable compared to the distorted conformation of $S_{C\ min}$ (Supplementary Fig. 46). Therefore, $S_{A\ min}$ is the lowest stationary point among all low-lying excited singlet states in the solution phase. In the solid-phase ONIOM model, the amino group in the ground state ($S_{0\ min}$) formed three hydrogen bonds with the α-CD (Supplementary Fig. 47). These hydrogen bonds inhibited the formation of a stable conjugated structure of $S_{A\ min}$, thereby increased its energy and reversed the energy order of $S_{C\ min}$ and $S_{A\ min}$ (Supplementary Figs. 48–51). Second, under the solid-phase ONIOM model, the $S_{C\ min}$ can undergo relaxation to the $T_{A\ min}$ via the $MECP_{SC/TA}$ pathway. However, in aqueous solution, our calculations show that the

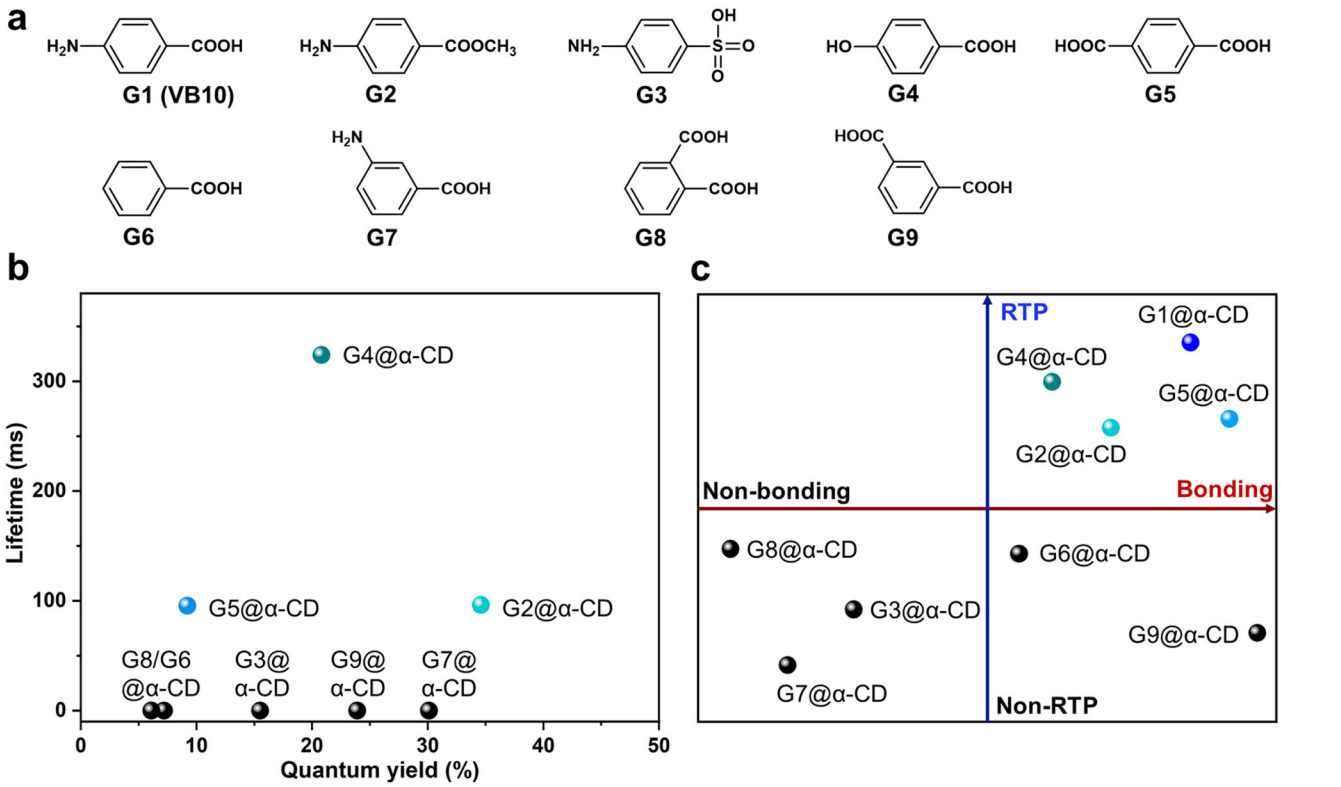

Fig. 5 | Binding with guest compounds. a Structures of guests G1 – G9. **b** Lifetime (τ) and quantum yield (Φ) of G2 – G9/α-CD (Inset: luminescence photographs of G1 – G9/α-CD under 254 nm and after ceasing irradiation). **c** Relationship between bonding capacity and phosphorescence properties of G1-G9/α-CD.

$S_{A\ min}$ lacks any accessible low-energy $MECP_{SA/TA}$ route, thereby preventing this relaxation process. Speculative analyses of the possible reasons why the $MECP_{SA/TA}$ point could not be located are provided in the Supplementary Information (Supplementary Figs. 41 and 42). It is evident that in the solution state, the main absorbing excited state $S_{A\ min}$ is also the lowest stationary point among all low-lying excited singlet states, making the fluorescence process a more favorable process (the relative energy is 102.5 kcal/mol for $S_{A\ min}$ and 110.7 kcal/mol for $S_{C\ min}$). In the solid state, the hydrogen bonds between the host α-CD and the guest VB10 raise the energy of $S_{A\ min}$, making the lower-energy $S_{C\ min}$ more readily relax to the T_A state via $MECP_{SC/TA}$, thereby promoting the phosphorescence process.

Since VB10 (G1) possessed an electron-donating group of amino group and an electron-withdrawing group of carboxyl group, we evaluated other guests (G2 – G10) to further reveal the relationship between structures and phosphorescence properties (Fig. 5a). After replacing the carboxyl group by carboxylic ester (G2) and sulfoacid (G3), the resulted G2/α-CD showed a dual emission of fluorescence (λ_{max} = 335 nm, τ = 0.90 ns) and phosphorescence (λ_{max} = 420 nm, τ = 96.3 ms) and a PLQY of 34.6%, which is inferior to the VB10@α-CD both in lifetime and quantum yield (Supplementary Figs. 52–54). For G3/α-CD, no phosphorescence was observed (Fig. 5b and Supplementary Figs. 55 and 56). These results revealed that carboxyl group is crucial for the phosphorescence of supramolecules. We then replaced amino group by hydroxyl (G4), carboxyl (G5), and removed it (G6). Both G4/α-CD and G5/α-CD showed obvious phosphorescence (λ_{max} = 414 nm, τ = 324 ms, PLQY = 20.8% for G4/α-CD; λ_{max} = 417 nm, τ = 95.6 ms, PLQY = 9.2% for G5/α-CD) (Supplementary Figs. 57–62). While G6/α-CD have no phosphorescence (Supplementary Figs. 63 and 64). These results indicated that amino group can be replaced by other groups but cannot be removed. We further investigated the influence of positional isomerization of functional groups by comparing *m*-aminobenzoic acid (G7) with VB10 (*p*-aminobenzoic acid) and comparing *o*/*m*/*p*-benzenedicarboxylic acid (G8, G9 and G5) with each other. It should be pointed out that *o*-aminobenzoic acid is unavailable because of its one of role as drug raw materials. Different from the intense phosphorescence of VB10@α-CD, the G7/α-CD have no phosphorescence (Supplementary Figs. 65 and 66). This also occurred in the G8, G9 and G5. Both G8/α-CD and G9/α-CD have no phosphorescence, while G5/α-CD exhibited blue phosphorescence (Supplementary Figs. 67–70). These results verified that positional isomerization of functional groups have great influence on the phosphorescence of supramolecules, and the para-position is the best. As a comparison, the photophysical properties of guests (G2 – G9) were also investigated and all of them showed weak emission without any phosphorescence excepted G4 (Supplementary Figs. 71–87 and Supplementary Table 3).

The origin of these differences in phosphorescence properties caused by replacing substituents or changing positions were further clarified by ^{1}H NMR and ITC methods. After titrating with α-CD, guests G2, G4 – G6 and G9 showed obvious chemical shifts and K_a range of (0.68 – 5.2) × 10^3 M^{-1}, indicated the formation of host–guest complexes guests@α-CD (G2@α-CD, G4@α-CD, G5@α-CD, G6@α-CD, and G9@α-CD) (Supplementary Figs. 88–97 and Supplementary Table 4). For G3, G7 and G8, no thermal change was observed in the ITC measurements although there were tiny chemical shifts in the ^{1}H NMR spectra, revealing the non-bonding between these guests and α-CD (Supplementary Figs. 98–103 and Supplementary Table 4). Interestingly, only guests (G1 – 2, G4 – G5 and G9) that can be encapsulated by α-CD showed phosphorescence, confirming that the formation of supramolecule with α-CD is the essential requirement for the turning on the phosphorescence (Fig. 5c).

α-CD was replaced by larger hosts of β-CD and γ-CD to evaluate the influence of size effect for the phosphorescence of supramolecules. In the solid state, VB10/β-CD exhibited a bright blue luminescence and displayed a persistent blue afterglow up to 6 s after ceasing the 254 nm UV irradiation (Supplementary Fig. 104). The PL spectra,

https://doi.org/10.1038/s41467-026-69431-y

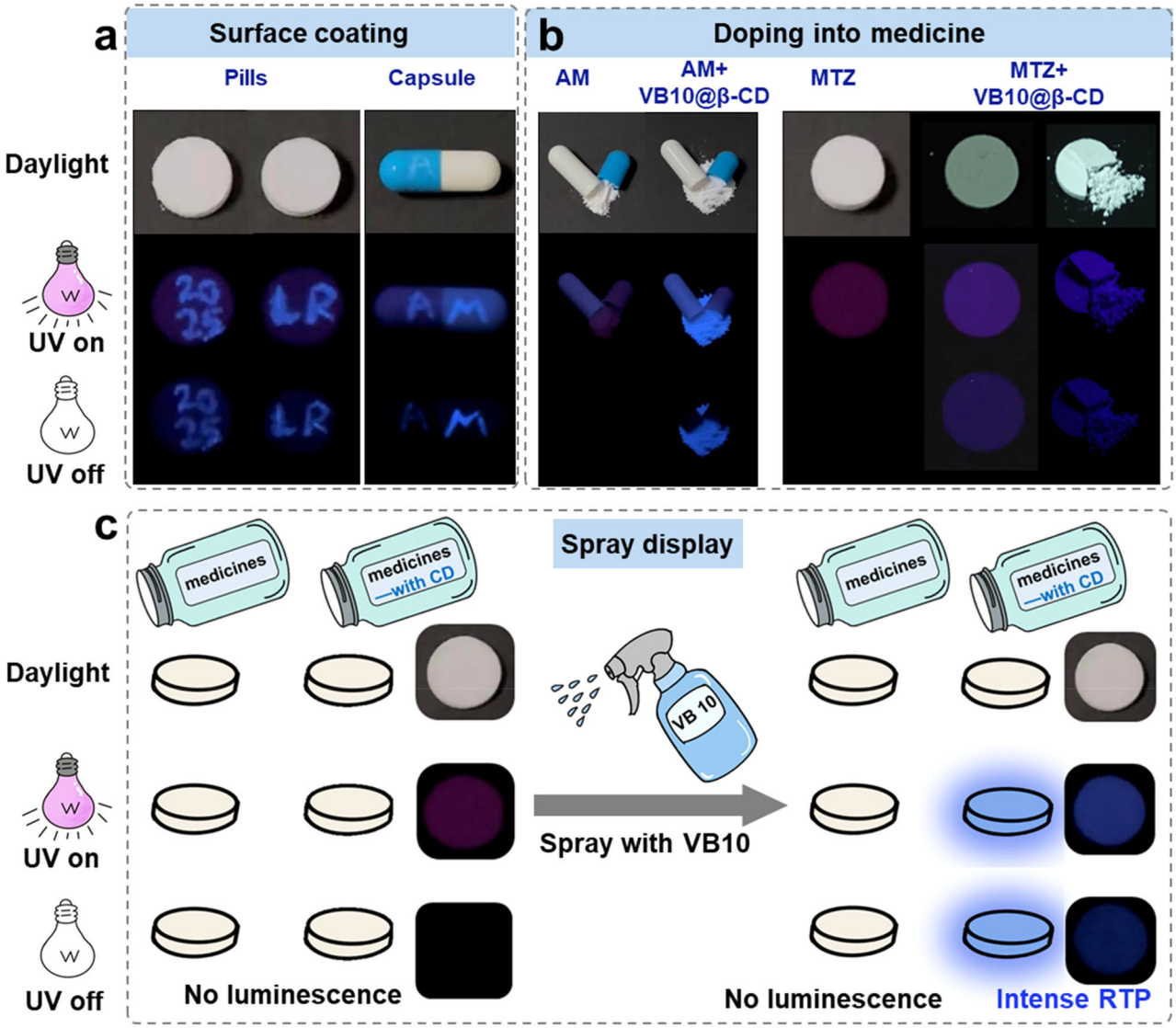

Fig. 6 | Medicine anticounterfeiting by three methods of surface coating, doping into medicine, and spray display. a Surface coating: coat information onto the surface of pills by aqueous solution of VB10@β-CD. **b** Doping into medicine: dope powder of VB10@β-CD into capsule or pills. **c** Spray display: dope β-CD into pills and then spray aqueous solution of VB10).

delayed PL spectra, and time-resolved PL decay curves proved the dual emission of phosphorescence (λ_{max} = 434 nm, τ = 1.16 s) and fluorescence (λ_{max} = 335 nm, τ = 1.17 ns), with a PLQY of 86.5% (Supplementary Figs. 105–107). The identical emission peaks, and similar lifetime and quantum yields revealed that the larger host β-CD could also provide similar circumstance for VB10 with that of α-CD. The circular dichroism spectra of VB10/β-CD showed opposite Cotton effect both in the solid state and in aqueous solution (Supplementary Fig. 108). Moreover, VB10/β-CD exhibited positive CPL, with a $|g_{lum}|$ value of 3.6×10^{-3} (Supplementary Fig. 109). For γ-CD/VB10, no phosphorescence could be observed, possible because of unfavorable complexation (Supplementary Figs. 110 and 111). These hypotheses were further proven by ^{1}H NMR spectra and ITC experiments. β-CD could encapsulate VB10 to form a supramolecule VB10@β-CD and showed a K_a of $(7.5 \pm 0.4) \times 10^2\,M^{-1}$ (Supplementary Figs. 112 and 113). No detectable thermal change was observed after titrating VB10 with γ-CD, although there were chemical shifts in ^{1}H NMR spectra, indicating the weak interaction between them (Supplementary Figs. 114 and 115). These results verified the importance of size matching between hosts and VB10 and further confirmed the requirement of host–guest complexation for turning on phosphorescence.

The obtained edible phosphorescent supramolecules VB10@α/β-CD have the advantages of high performance, low cost, and good robustness. Therefore, we verified their applications in medicine anticounterfeiting. As aforementioned, encrypting and printing information on or into pills and capsules is an advanced and effective method because medicines can be authenticated independent of the packaging. We explored three methods of surface coating, doping into medicine, and spray display to verify medicine anticounterfeiting. For surface coating, aqueous solution of VB10@β-CD was utilized as a phosphorescent ink to paint on the surface of pills, and no information could be found under daylight. Under the irradiation of 254 nm, labeled "2025" and "LR" appeared (Fig. 6a). They are clearer after ceasing irradiation because background autofluorescence interference from medicine no longer exists. Similarly, this phosphorescent ink can also be used for labeling capsules. Printing the "AM" and "CA" on the surface of amoxicillin (AM) and cephalosporin (CA) capsules by VB10@β-CD, the authenticity of the medicines can only be identified after ceasing irradiation and neither under daylight nor UV lamps (Fig. 6a and Supplementary Fig. 116a). In addition, doping VB10@β-CD into capsule or pills is another method for medicine anticounterfeiting. After mixing small amount (2 mg) of VB10@β-CD powder into

medicine AM or MTZ, the obtained capsule and pill displayed persistent blue afterglow after removing the UV irradiation, while the unlabeled contrasts have no such afterglow (Fig. 6b). Interestingly, the afterglow can only be excited by UV wavelength below 320 nm but not long wavelength such as 365 nm, which provided additional guarantee for anticounterfeiting (Supplementary Fig. 116b). Even the pill was chopped, each part of the pill emitted a persistent blue light (Fig. 6b and Supplementary Fig. 116c). The third method is spray display on medicine. Since the encapsulation is the requirement for turning on RTP, β-CD as one of components can be premixed into the pills and the prepared medicine cannot be detected with luminescence except the autofluorescence. Then the medicine authenticity can only be identified by spraying aqueous solution of another component (VB10) which can be co-packaged with medicine (Fig. 6c). This anticounterfeiting cannot be cloned by other methods such as premixing phosphorescent materials into medicine, therefore ensuring high safety. Moreover, the good CPL phosphorescence qualified the supramolecules as useful systems for chiral anticounterfeiting.

Discussion

In summary, we have successfully prepared a class of edible phosphorescent supramolecules, namely VB10@α/β-CD, through the host−guest complexation between easily available α/β-CD and VB10. These phosphorescence supramolecules could be obtained via concisely grinding α/β-CD and VB10 with water or co-crystallization from aqueous solution. They exhibit a long phosphorescence lifetime of up to 1.16 s, a high PL quantum yield of up to 86.5%, and a bright blue afterglow lasting up to 6 s after ceasing the irradiation of UV light. Moreover, VB10@α-CD shows dual circularly polarized luminescence of fluorescence and phosphorescence, with $|g_{lum}|$ values of up to 1.5×10^{-2} and 7.5×10^{-3}, respectively. The phosphorescence remains even when the ratio of VB10 to CD is as low as 1:1000 because of the excellent encapsulation of α/β-CD for VB10. Both the structures of guests and size effect of hosts have an important influence on the phosphorescence performance of host−guest complexes. The crucial roles of non-radiative process for the phosphorescence in the solid state are clearly revealed by complete theoretical calculations. The encapsulation of α/β-CD reverses the energy ordering of VB10's excited singlet states, promotes the formation of the minimum energy crossing point (MECP) between singlet state and triplet state, and therefore enhances phosphorescence. Our case study demonstrates that: 1) By combining the ONIOM method with the MECP-efficient locating algorithm, TDDFT can achieve at least semi-quantitative accuracy. 2) It is feasible to provide a detailed description of the photophysical processes in large organic molecular/supramolecular systems in the solid state and to elucidate their luminescence mechanisms. Moreover, the good moisture robustness, room-temperature phosphorescence and circularly polarized luminescence make VB10@β-CD edible phosphorescent inks for in-medicine anticounterfeiting. Three anticounterfeiting methods of surface coating, doping into medicine, and spray display are well verified for both pills and capsules. Thus, the present set of phosphorescent supramolecules provide a typical example for constructing phosphorescent materials and may see use in high-safety medicine anticounterfeiting.

Methods

Materials

All reagents and solvents were obtained commercially and used without further purification, unless otherwise noted.

Measurements

^{1}H NMR spectra were recorded on Bruker Avance III 400 MHz instrument. Single crystal X-ray data were collected by direct methods using a Bruker SMART APEX II diffractometer. Photoluminescence spectra and lifetime were obtained on FLS 1000 and HAMAMATSU C16361-01. Fluorescence and phosphorescence quantum yields were measured on HAMAMATSU Quantaurus-QY plus. ITC experiments were performed on MicroCal PEAQ-ITC instrument. CPL spectra were measured on JASCO CPL-300 spectrophotometer. CD spectra were measured on JASCO J-815 spectrophotometer.

Crystal structure of VB10@α-CD

A mixed aqueous solution (2 mL) of VB10 (5×10^{-2} mol/L) and α-CD (5×10^{-2} mol/L) was passed through a 0.22 μm filter. After a slow evaporation of the solution for 6 days, colorless block crystals were obtained.

Data availability

The authors declare that the data supporting the findings of this study are available within the article and its Supplementary Information. Data are available from the corresponding author upon request.

References

1. Aldhous, P. Murder by medicine. *Nature* **434**, 132–134 (2005).
2. Pyzik, O. Z. & Abubakar, I. Fighting the fakes: Tackling substandard and falsified medicines. *Nat. Rev. Dis. Prim.* **8**, 55 (2022).
3. A study on the public health and socioeconomic impact of substandard and falsified medical products. World Health Organization https://iris.whoint/handle/10665/331690 (2017).
4. Deisingh, A. K. Pharmaceutical counterfeiting. *Analyst* **130**, 271–279 (2005).
5. Kovacs, S. et al. Technologies for detecting falsified and substandard drugs in low and middle-income countries. *PLOS One* **9**, e90601 (2014).
6. Zhang, H. et al. Materials and technologies to combat counterfeiting of pharmaceuticals: Current and future problem tackling. *Adv. Mater.* **32**, 1905486 (2020).
7. Leem, J. W. et al. Edible matrix code with photogenic silk proteins. *ACS Cent. Sci.* **8**, 513–526 (2022).
8. Mackey, T. K. & Nayyar, G. A review of existing and emerging digital technologies to combat the global trade in fake medicines. *Expert Opin. Drug Saf.* **16**, 587–602 (2017).
9. Leem, J. W. et al. Edible unclonable functions. *Nat. Commun.* **11**, 328 (2020).
10. Kretschmer, J. et al. Paramagnetic encoding of molecules. *Nat. Commun.* **13**, 3179 (2022).
11. Peng, Y. et al. Edible ultralong organic phosphorescent excipient for afterglow visualizing the quality of tablets. *Adv. Mater.* **36**, 2406618 (2024).
12. Abdollahi, A., Roghani-Mamaqani, H., Razavi, B. & Salami-Kalajahi, M. Photoluminescent and chromic nanomaterials for anticounterfeiting technologies: Recent advances and future challenges. *ACS Nano* **14**, 14417–14492 (2020).
13. Zhang, F. et al. Multimodal, convertible, and chiral optical films for anti-counterfeiting labels. *Adv. Funct. Mater.* **32**, 2204487 (2022).
14. You, M. et al. Three-dimensional quick response code based on inkjet printing of upconversion fluorescent nanoparticles for drug anti-counterfeiting. *Nanoscale* **8**, 10096–10104 (2016).
15. Szejtli, J. Introduction and general overview of cyclodextrin chemistry. *Chem. Rev.* **98**, 1743–1754 (1998).
16. Crini, G. Review: A history of cyclodextrins. *Chem. Rev.* **114**, 10940–10975 (2014).
17. Davis, M. E. & Brewster, M. E. Cyclodextrin-based pharmaceutics: Past, present and future. *Nat. Drug Discov.* **3**, 1023–1035 (2004).
18. Jansook, P., Ogawa, N. & Loftsson, T. Cyclodextrins: Structure, physicochemical properties and pharmaceutical applications. *Int. J. Pharm.* **535**, 272–284 (2018).
19. Rekharsky, M. V. & Inoue, Y. Complexation thermodynamics of cyclodextrins. *Chem. Rev.* **98**, 1875–1918 (1998).

20. Liu, Y. & Chen, Y. Cooperative binding and multiple recognition by bridged bis(β-cyclodextrin)s with functional linkers. *Acc. Chem. Res.* **39**, 681–691 (2006).
21. Harada, A., Takashima, Y. & Nakahata, M. Supramolecular polymeric materials via cyclodextrin–guest interactions. *Acc. Chem. Res.* **47**, 2128–2140 (2014).
22. Dsouza, R. N., Pischel, U. & Nau, W. M. Fluorescent dyes and their supramolecular host/guest complexes with macrocycles in aqueous solution. *Chem. Rev.* **111**, 7941–7980 (2011).
23. Zhang, Q.-W. et al. Multicolor photoluminescence including white-light emission by a single host–guest complex. *J. Am. Chem. Soc.* **138**, 13541–13550 (2016).
24. Zhou, W.-L., Lin, W., Chen, Y. & Liu, Y. Supramolecular assembly confined purely organic room temperature phosphorescence and its biological imaging. *Chem. Sci.* **13**, 7976–7989 (2022).
25. Shigemitsu, H. et al. Cyclodextrins with multiple pyrenyl groups: An approach to organic molecules exhibiting bright excimer circularly polarized luminescence. *Angew. Chem. Int. Ed.* **61**, e202114700 (2022).
26. Tu, C. et al. Host–guest complexation-induced aggregation based on pyrene-modified cyclodextrins for improved electronic circular dichroism and circularly polarized luminescence. *Angew. Chem. Int. Ed.* **61**, e202203541 (2022).
27. Song, X., Zhu, X., Qiu, S., Tian, W. & Liu, M. Self-assembly of adaptive chiral [1]rotaxane for thermo-rulable circularly polarized luminescence. *Angew. Chem. Int. Ed.* **61**, e202208574 (2022).
28. Kazem-Rostami, M. et al. Helically chiral hybrid cyclodextrin metal–organic framework exhibiting circularly polarized luminescence. *J. Am. Chem. Soc.* **144**, 9380–9389 (2022).
29. Kacsó, I., Borodi, G., Farcas, S. I., Hernanz, A. & Bratu, I. Host–guest system of Vitamin B10 in β-cyclodextrin: Characterization of the interaction in solution and in solid state. *J. Incl. Phenom. Macrocycl. Chem.* **68**, 175–182 (2010).
30. Elasaad, K., Norberg, B. & Wouters, J. Crystallographic, UV spectroscopic and computational studies of the inclusion complex of α-cyclodextrin with p-aminobenzoic acid. *Supramol. Chem.* **24**, 312–324 (2012).
31. Peng, C. et al. Afterglow carbon dots: From fundamentals to applications. *Research* **2021**, 6098925 (2021).
32. Jiang, K., Wang, Y., Gao, X., Cai, C. & Lin, H. Facile, quick, and gram-scale synthesis of ultralong-lifetime room-temperature-phosphorescent carbon dots by microwave irradiation. *Angew. Chem. Int. Ed.* **57**, 6216–6220 (2018).
33. Shao, W. & Kim, J. Metal-free organic phosphors toward fast and efficient room-temperature phosphorescence. *Acc. Chem. Res.* **55**, 1573–1585 (2022).
34. An, Z. et al. Stabilizing triplet excited states for ultralong organic phosphorescence. *Nat. Mater.* **14**, 685 (2015).
35. Gong, Y. et al. Crystallization-induced phosphorescence of benzils at room temperature. *Sci. Chin. Chem.* **56**, 1183–1186 (2013).
36. Zhao, W., He, Z. & Tang, B. Z. Room-temperature phosphorescence from organic aggregates. *Nat. Rev. Mater.* **5**, 869–885 (2020).
37. Li, Q. & Li, Z. Molecular packing: Another key point for the performance of organic and polymeric optoelectronic materials. *Acc. Chem. Res.* **53**, 962–973 (2020).
38. Kabe, R. & Adachi, C. Organic long persistent luminescence. *Nature* **550**, 384–387 (2017).
39. Guo, J., Yang, C. & Zhao, Y. Long-lived organic room-temperature phosphorescence from amorphous polymer systems. *Acc. Chem. Res.* **55**, 1160–1170 (2022).
40. Gao, R., Kodaimati, M. S. & Yan, D. Recent advances in persistent luminescence based on molecular hybrid materials. *Chem. Soc. Rev.* **50**, 5564–5589 (2021).
41. Yan, X. et al. Recent advances on host–guest material systems toward organic room temperature phosphorescence. *Small* **18**, 2104073 (2022).
42. Gan, N., Shi, H., An, Z. & Huang, W. Recent advances in polymer-based metal-free room-temperature phosphorescent materials. *Adv. Funct. Mater.* **28**, 1802657 (2018).
43. Ma, X., Xu, C., Wang, J. & Tian, H. Amorphous pure organic polymers for heavy-atom-free efficient room-temperature phosphorescence emission. *Angew. Chem. Int. Ed.* **57**, 10854–10858 (2018).
44. Li, H. et al. Achieving stimuli-responsive amorphous organic afterglow in single-component copolymer through self-doping. *J. Am. Chem. Soc.* **145**, 7343–7351 (2023).
45. Li, D. et al. Amorphous metal-free room-temperature phosphorescent small molecules with multicolor photoluminescence via a host–guest and dual-emission strategy. *J. Am. Chem. Soc.* **140**, 1916–1923 (2018).
46. Ma, X., Wang, J. & Tian, H. Assembling-induced emission: An efficient approach for amorphous metal-free organic emitting materials with room-temperature phosphorescence. *Acc. Chem. Res.* **52**, 738–748 (2019).
47. Dai, X.-Y., Huo, M. & Liu, Y. Phosphorescence resonance energy transfer from purely organic supramolecular assembly. *Nat. Rev. Chem.* **7**, 854–874 (2023).
48. Ma, X.-K. & Liu, Y. Supramolecular purely organic room-temperature phosphorescence. *Acc. Chem. Res.* **54**, 3403–3414 (2021).
49. Garain, S., Garain, B. C., Eswaramoorthy, M., Pati, S. K. & George, S. J. Light-harvesting supramolecular phosphors: Highly efficient room temperature phosphorescence in solution and hydrogels. *Angew. Chem. Int. Ed.* **60**, 19720–19724 (2021).
50. Li, D. et al. Ultralong room-temperature phosphorescence with second-level lifetime in water based on cyclodextrin supramolecular assembly. *ACS Nano* **17**, 12895–12902 (2023).
51. Gu, T. et al. Non-covalent iron-armored chain horse: A strategy leading to highly efficient deep-blue room temperature phosphorescence. *Adv. Opt. Mater.* **12**, 2400920 (2024).
52. Tang, S. et al. Nonconventional luminophores: Characteristics, advancements and perspectives. *Chem. Soc. Rev.* **50**, 12616–12655 (2021).
53. Alam, P. et al. Organic long-persistent luminescence from a single-component aggregate. *J. Am. Chem. Soc.* **144**, 3050–3062 (2022).
54. Peng, Q., Ma, H. & Shuai, Z. Theory of long-lived room-temperature phosphorescence in organic aggregates. *Acc. Chem. Res.* **54**, 940–949 (2021).
55. Ma, H., Peng, Q., An, Z., Huang, W. & Shuai, Z. Efficient and long-lived room-temperature organic phosphorescence: Theoretical descriptors for molecular designs. *J. Am. Chem. Soc.* **141**, 1010–1015 (2019).
56. Adamo, C. & Jacquemin, D. The calculations of excited-state properties with time-dependent density functional theory. *Chem. Soc. Rev.* **42**, 845–856 (2013).
57. Kwon, M. S. et al. Suppressing molecular motions for enhanced room-temperature phosphorescence of metal-free organic materials. *Nat. Commun.* **6**, 8947 (2015).
58. Zhu, T., Yang, T., Zhang, Q. & Yuan, W. Z. Clustering and halogen effects enabled red/near-infrared room temperature phosphorescence from aliphatic cyclic imides. *Nat. Commun.* **13**, 2658 (2022).
59. Nelson, T. R. et al. Non-adiabatic excited-state molecular dynamics: Theory and applications for modeling photophysics in extended molecular materials. *Chem. Rev.* **120**, 2215–2287 (2020).
60. Matsika, S. Electronic structure methods for the description of nonadiabatic effects and conical intersections. *Chem. Rev.* **121**, 9407–9449 (2021).

61. Liu, Y., Zhao, Y.-L., Chen, Y. & Guo, D.-S. Assembly behavior of inclusion complexes of β-cyclodextrin with 4-hydroxyazobenzene and 4-aminoazobenzene. *Org. Biomol. Chem.* **3**, 584–591 (2005).

Acknowledgements

The authors gratefully acknowledge the National Natural Science Foundation of China (22201211, 22471194, and 21971192) and the Natural Science Foundation of Tianjin City (23JCZDJC00660 and 20JCZDJC00200).

Author contributions

W.-T. W. and C.-Y. D. contributed equally to this work. Z.-Y. Z., Y. Z., and C. L. conceived this project and designed the experiments. W.-T. W., C.-Y. D. and Y.-Y. Z. assisted in analytical testing and data collection. K. L. performed the calculations. W.-T.W. and Z.-Y. Z. wrote the manuscript. Z.-Y. Z., K. L., Y. Z., and C. L. revised and finalized the manuscript.

Competing interests

The authors declare that they have no competing interests.

Additional information

Supplementary information The online version contains supplementary material available at https://doi.org/10.1038/s41467-026-69431-y.

Correspondence and requests for materials should be addressed to Zhi-Yuan Zhang, Kun Liu, Yanli Zhao or Chunju Li.

Peer review information *Nature Communications* thanks Zong-Quan Wu and the other, anonymous, reviewers for their contribution to the peer review of this work. A peer review file is available.